J. Fluid Mech. (1990), vol. 221, pp. 533–552
Printed in Great Britain

Axisymmetric vortex breakdown Part 1. Confined swirling flow

By J. M. LOPEZ
Aeronautical Research Laboratory, P.O. Box 4331, Melbourne, Vic., 3001, Australia

(Received 7 August 1986 and in revised form 14 May 1990)

A comparison between the experimental visualization and numerical simulations of the occurrence of vortex breakdown in laminar swirling flows produced by a rotating endwall is presented. The experimental visualizations of Escudier (1984) were the first to detect the presence of multiple recirculation zones and the numerical model presented here, consisting of a numerical solution of the unsteady axisymmetric Navier–Stokes equations, faithfully reproduces these phenomena and all other observed characteristics of the flow. Further, the numerical calculations elucidate the onset of oscillatory flow, an aspect of the flow that was not clearly resolved by the flow visualization experiments. Part 2 of the paper examines the underlying physics of these vortex flows.

1. Introduction

Vortex breakdown in swirling flows has been the subject of much attention since it was first recognized in the tip vortices of delta-winged aircraft (Peckham & Atkinson 1957). More recently it has emerged as a serious problem at high angle of attack for highly manoeuvrable military aircraft. As yet, there is no general consensus on the physical mechanisms responsible for its occurrence. The term vortex breakdown is associated with an abrupt change in the character of a columnar vortex at some axial station. It is usually observed as a sudden widening of the vortex core together with a deceleration of the axial flow and is often followed by a region or regions of recirculation.

The work reported here and in Part 2 (Brown & Lopez 1990) is a part of a larger programme (Lopez 1988 and Brown & Lopez 1988) to develop further an understanding of vortex breakdown, particularly as it relates to highly manoeuvrable aircraft.

Experimental studies of vortex breakdown over delta-winged aircraft have been severely hampered by the sensitivity of the flow to the presence of external probes, making quantitative measurements of the flow in the 'burst' regions much more difficult. Further complications arise as a result of the large number of parameters involved, some of which are difficult to measure and/or control and whose importance to the mechanisms leading to vortex breakdown is not known. With the identification of the vortex breakdown of swirling flows in cylindrical tubes (Harvey 1960), a large number of experimental investigations were undertaken (e.g. Sarpkaya 1971; Faler & Leibovich 1978; Escudier & Zehnder 1982). A number of distinctive forms of breakdown were observed in these investigations, which also showed the phenomenon typically to be unsteady and possessing various degrees of turbulence and asymmetry. From these results, it had been assumed that a description of vortex breakdown would require a three-dimensional, time-dependent calculation of the

Navier–Stokes equations, albeit with the possibility at high Reynolds numbers of modelling the small-scale turbulence. Early attempts to model this swirling pipe flow, however, were restricted to the axisymmetric time-independent Navier–Stokes equations. Calculations using these equations by Grabowski & Berger (1976) gave numerical solutions depicting a closed recirculation zone, very similar to the 'axisymmetric' breakdown bubbles found by Harvey (1960) and Sarpkaya (1971). It has not been shown whether these solutions to the time-independent equations are steady solutions of the time-dependent equations. Further discussion of the numerical simulation of the swirling pipe flow is deferred to §3 of Part 2. Comprehensive literature reviews by Hall (1972), Leibovich (1978, 1984) and Escudier (1986, 1988) give extensive accounts of the experimental, theoretical and numerical work on vortex breakdown.

Escudier (1984) observed the phenomenon of vortex breakdown in swirling flows in a cylindrical container with a rotating endwall, using a laser-induced-fluorescence technique. The experimental results extended those obtained earlier by Vogel (1968) and Ronnenberg (1977) and are the first to be reported in which multiple breakdown bubbles exist in the closed cylindrical geometry. The recirculation bubbles were observed to be axisymmetric and steady over a large range of the governing parameters, which reinforced Escudier's (1984) view, earlier expressed as a result of a series of swirling pipe flow experiments (Escudier & Keller 1983), that vortex breakdown in general is inherently axisymmetric and that departures from axial symmetry result from instabilities not directly associated with the breakdown process. Escudier's experiments provide a particularly well-defined set of flows in which vortex breakdown occurs. They are mathematically well posed, especially with regard to the boundary conditions. His figures (1984) motivated the present study in which the Navier–Stokes equations are solved numerically under the assumption of axial symmetry. A principal aim of this initial study was to clarify whether, under the assumption of axial symmetry, the numerical solutions accurately reproduce all of the observed flow characteristics reported by Escudier (1984).

A further motivation for undertaking the investigation was to develop a more detailed understanding of the physics of the flow and to clarify features that were not readily resolved from the visualizations. For example, the dye streaks are 'blurred' in the region of critical points in the experiment and the nature of the downstream end of the recirculation bubble is difficult to ascertain from flow visualization. A main reason for this 'blurred' picture is dye diffusion but, in some cases Escudier (1984) noted that certain recirculation zones never develop a well-defined internal structure. The numerical study shows that these regions in fact possess a localized low-frequency unsteadiness and this unsteadiness would result in a 'blurred' flow visualization.

In Part 2 of this study the physics of the flows is examined in more detail. The vortex breakdown phenomenon is viewed from a new perspective. Instead of concentrating on the stream function or the velocity and pressure field as has been common in the past (e.g. Squire 1960; Benjamin 1962), emphasis is placed on the azimuthal component of vorticity. An explanation of the vortex breakdown phenomenon is given based on the behaviour of the azimuthal vorticity. The mechanics of vortex breakdown in this particular geometry suggests a generalization to other geometries. This is discussed in Part 2 for the further case of swirling pipe flow.

Previous numerical studies of swirling flows confined within a cylindrical container (e.g. Pao 1970; Lugt & Haussling 1973; Dijkstra & Heijst 1983) have either been

restricted to small-aspect-ratio flows (H/R, ratio of height and radius of the cylinder, less than 1), or flows with Re, the rotational Reynolds number, too small for vortex breakdown to occur. Lugt & Haussling (1982) is a notable exception in which $H/R < 1.6$, and the occurrence of a single breakdown bubble is reported. Their computational mesh does not appear to be fine enough, however, since they found the size and location of the bubble to vary as the resolution was altered and the timescales of their solutions are not consistent with experimental observations.

Since the first version of this paper was submitted, Lugt & Abboud (1987) have also published numerical computations of the vortex breakdown phenomenon produced in an enclosed cylinder by a rotating endwall. Their calculations and those presented here overlap somewhat as both studies use the available experimental results of Escudier (1984) as comparisons for the numerical calculations. The results presented by Lugt & Abboud (1987) generally agree very well with those presented here but their numerical method of integrating the governing equations is quite different to the present method. A large number of their results had not been integrated forward until a true steady state had been reached and no information regarding the distribution of the azimuthal component of vorticity is presented, which is shown in Part 2 of this study to be particularly significant in developing an understanding of the physical mechanism responsible for the vortex breakdown of the vortical core flow.

2. Governing equations and boundary conditions

The flows of interest are simulated by considering a cylinder of radius R and length H, the bottom endwall of which is impulsively started to rotate at constant angular velocity Ω. The fluid, which completely fills the cylinder, is incompressible, of uniform density and a constant kinematic viscosity ν. The axisymmetric form of the Navier–Stokes equations, in cylindrical coordinates (r, ϕ, z) with corresponding velocity components (u, v, w), is employed. Time and length are scaled by Ω and $1/R$ respectively.

The system of equations is solved by employing the stream-function–vorticity formulation, where the pressure does not appear explicitly. This is achieved by the introduction of a stream function ψ, where

$$u = -\frac{1}{r}\frac{\partial \psi}{\partial z}, \quad w = \frac{1}{r}\frac{\partial \psi}{\partial r}, \tag{1}$$

which satisfies continuity and gives for the azimuthal component of vorticity

$$\eta = -\frac{1}{r}\frac{\partial^2 \psi}{\partial z^2} - \frac{\partial}{\partial r}\left(\frac{1}{r}\frac{\partial \psi}{\partial r}\right). \tag{2}$$

Incorporating (1) and(2) in the Navier–Stokes equations leads to the following prediction equations for the azimuthal components of velocity and vorticity together with the prognostic equation for the stream function:

$$\frac{\partial v}{\partial t} = \frac{1}{r}\mathrm{J}(v) + \frac{1}{r}\frac{v}{r}\frac{\partial \psi}{\partial z} + \frac{1}{Re}\left[\frac{\partial^2 v}{\partial z^2} + \frac{\partial^2 v}{\partial r^2} + \frac{1}{r}\frac{\partial v}{\partial r} - \frac{v}{r^2}\right], \tag{3}$$

$$\frac{\partial \eta}{\partial t} = \mathrm{J}\left(\frac{\eta}{r}\right) + 2\frac{v}{r}\frac{\partial v}{\partial z} + \frac{1}{Re}\left[\frac{\partial^2 \eta}{\partial z^2} + \frac{\partial^2 \eta}{\partial r^2} + \frac{1}{r}\frac{\partial \eta}{\partial r} - \frac{\eta}{r^2}\right], \tag{4}$$

and
$$\frac{\partial^2\psi}{\partial z^2}+\frac{\partial^2\psi}{\partial r^2}-\frac{1}{r}\frac{\partial\psi}{\partial r}=-r\eta, \tag{5}$$

where
$$Re=\frac{\Omega R^2}{\nu},$$

and
$$\mathrm{J}=\frac{\partial\psi}{\partial z}\frac{\partial}{\partial r}-\frac{\partial\psi}{\partial r}\frac{\partial}{\partial z}.$$

The boundary conditions relevant to the experiments of Escudier (1984) to complete the system (3)–(5) are

$$\left.\begin{aligned}
\psi=v=\eta=0 \quad & (r=0, \quad 0\leqslant z\leqslant H/R),\\
\psi=v=0, \quad \eta=-\frac{1}{r}\frac{\partial^2\psi}{\partial r^2} \quad & (r=1, \quad 0\leqslant z\leqslant H/R),\\
\psi=0, \quad v=r, \quad \eta=-\frac{1}{r}\frac{\partial^2\psi}{\partial z^2} \quad & (z=0, \quad 0\leqslant r\leqslant 1),\\
\psi=v=0, \quad \eta=-\frac{1}{r}\frac{\partial^2\psi}{\partial z^2} \quad & (z=H/R, \quad 0\leqslant r\leqslant 1).
\end{aligned}\right\} \tag{6}$$

The boundary condition at $r=0$ is due to the axial symmetry of the flow, the boundaries at $z=H/R$ and $r=1$ are rigid and stationary, while at $z=0$, the rigid endwall is in constant rotation for $t>0$. The fluid is stationary for $t\leqslant 0$.

3. Method of solution

The system of differential equations (3)–(5) are replaced by an approximating set of finite-difference equations, defined on a uniform mesh in the (r,z)-plane at times $n\Delta t$ $(n=0,1,2,\ldots)$. There are $(nr+1)\times(nz+1)$ grid nodes, and in all the cases presented here, the increments Δr and Δz are equal. Second-order-accurate centred differences are used to approximate all the spatial derivatives except those in the advection terms, where the Jacobian conserving difference operator J is approximated using a scheme due to Arakawa (1966). The time-differencing scheme used is that of Miller & Pearce (1974) which consists of alternate time-steps. For a prediction equation of the form $\partial F/\partial t=G(F)$, the odd time-steps are advanced according to

$$F^{*}=F^{n}+\Delta tG(F^{n}),$$
$$F^{n+1}=F^{n}+\Delta tG(F^{*}),$$

while for even time-steps

$$F^{n+1}=F^{n}+\Delta tG(F^{n}).$$

The prognostic equation (5) for the stream function is solved using the generalized cyclic reduction method of Sweet (1974).

To implement the boundary conditions for the azimuthal vorticity at the solid boundaries at time $(n+1)\Delta t$, the stream-function field at that time is needed. This is achieved by the following algorithm. First, the prediction equations (3) and (4) for v and η may be advanced to the next time-step $(n+1)\Delta t$ for the interior points since the prognostic equation (5) for ψ only requires knowledge of the interior values of η. From the solution to (5) together with the boundary conditions for ψ, the stream function is known everywhere at $t=(n+1)\Delta t$. The boundary values of η can now be

Re	H/R	nr	nz	$I(\eta)$	$I(\eta^+)$	$I(\eta^-)$
1256	1.5	40	60	−0.000386	0.12590	−0.12628
1256	1.5	60	90	−0.000175	0.12619	−0.12637
1492	1.5	40	60	−0.000418	0.12888	−0.12929
1492	1.5	60	90	−0.000188	0.12908	−0.12927
1854	1.5	40	60	−0.000461	0.13130	−0.13176
1854	1.5	60	90	−0.000206	0.13417	−0.13438
1994	2.5	60	150	−0.000237	0.15684	−0.15708
2126	2.5	60	150	−0.000244	0.15893	−0.15918
2126	2.5	100	250	−0.000175	0.16041	−0.16058
2889	3.5	60	210	−0.000277	0.18056	−0.18083
3023	2.5	60	210	−0.000286	0.18206	−0.18234

TABLE 1. Characteristics of the vorticity integral (η) for selected cases

estimated from ψ by noting that ψ and its normal derivative vanish at a rigid boundary. Hence, expanding ψ about the first point in from the boundary leads to

$$\eta(nr+1,j) = -2\psi(nr,j)/\Delta r^2,$$

$$\eta(i,1) = -2\psi(i,2)/(r\Delta z^2),$$

and

$$\eta(i,nz+1) = -2\psi(i,nz)/(r\Delta z^2).$$

Proper resolution of the boundary layers and any recirculation zones was ensured by the use of $\Delta r = \Delta z = 1/60$. A number of runs for $H/R = 1.5$ were performed using $\Delta r = \Delta z = 1/40$ with only slight differences in the outline of the recirculation zone being noted – the positions of the stagnation points were not appreciably altered by the reduction in resolution. One run at $H/R = 2.5$ and $Re = 2126$ implemented $\Delta r = \Delta z = 1/100$. The difference between the streamlines from these results and those from calculations with $\Delta r = \Delta z = 1/60$ were insignificant. All the calculations presented here are for $\Delta r = \Delta z = 1/60$ and $\Delta t = 0.05$, except for the one case of $H/R = 2.5$ and $Re = 2126$ where $\Delta r = \Delta z = 1/100$ and $\Delta t = 0.025$. In all cases, the stability of the model was ensured by the time-step satisfying both the Courant–Friedrichs–Lewy condition and the diffusion requirement (Williams 1967),

$$\Delta t < \tfrac{1}{8} Re\, \Delta r^2.$$

The quality of the numerical computations was further verified by (i) direct comparisons with experimental results (§4), and (ii) evaluation of the vorticity integral (Dijkstra & Heijst 1983). From the definition of the azimuthal vorticity (2), together with the boundary conditions, the stream function and its normal derivatives vanish on solid boundaries and $\psi = 0$ on the axis of symmetry, hence

$$\iiint_V r\eta \,\mathrm{d}V = 2\pi \int_{r=0}^{1} \int_{z=0}^{H/R} r^2 \eta \,\mathrm{d}z \,\mathrm{d}r = 0. \tag{7}$$

At $t = 1000$, this integral was evaluated by means of a two-dimensional trapezoidal rule, and the positive and negative contributions to the trapezoidal sum accumulated separately in $I(\eta^+)$ and $I(\eta^-)$ respectively. In the limit $\Delta r, \Delta z \to 0$, $I(\eta^+) + I(\eta^-) = 0$. The degree to which this is achieved is an indication of the quality of the numerical scheme. Table 1 lists the values of the integral (7) together with $I(\eta^+)$ and $I(\eta^-)$ for a selection of the cases considered. It is clear that the accuracy of the calculations is improved by increasing the resolution from $\Delta r, \Delta z = 1/40$ to $1/60$. For the case $Re = 1256$, $I_{\mathrm{rel}} = (I(\eta^-) + I(\eta^+))/(I(\eta^-) - I(\eta^+)) \approx 0.0015$ when $\Delta r, \Delta z = 1/40$, whereas

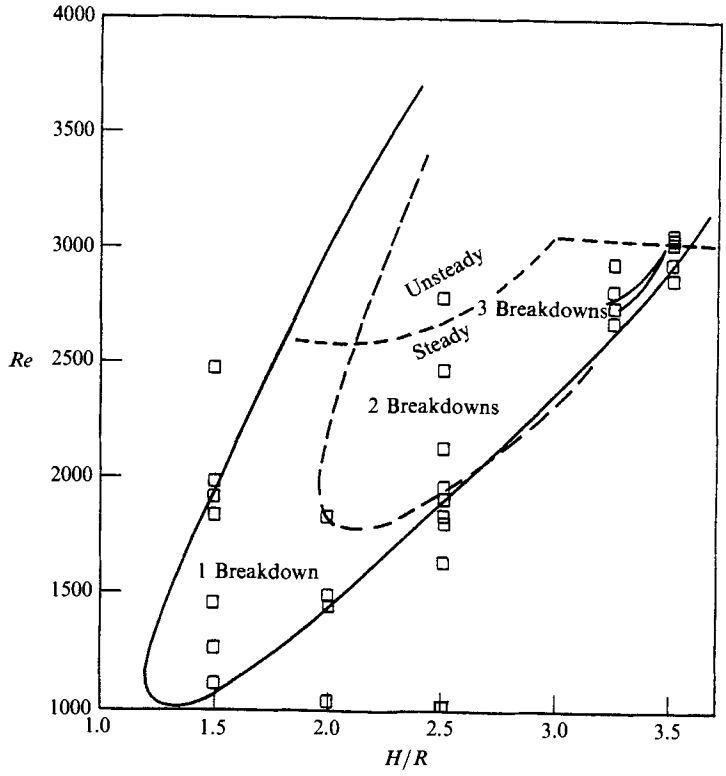

FIGURE 1. Stability boundaries for single, double and triple breakdowns, and boundary between steady and oscillatory flow, in the $(Re, H/R)$-plane (empirically determined by Escudier 1984). The locations in parameter space where the flow has been simulated are indicated by □.

$I_{\text{rel}} \approx 0.00069$ for $\Delta r, \Delta z = 1/60$. On further grid refinement, as illustrated by the $Re = 2126$ case, $I_{\text{rel}} \approx 0.00077$ for $\Delta r, \Delta z = 1/60$ and $I_{\text{rel}} \approx 0.00055$ for $\Delta r, \Delta z = 1/100$, indicating that $\Delta r, \Delta z = 1/60$ constitutes a good compromise between the level of accuracy and the computational effort required to achieve it. The extent to which the vorticity integral (7) is satisfied is reduced as Re is increased. However, in the Re-range considered, this trend is very weak, as when $Re = 1492$ and $\Delta r, \Delta z = 1/60$, $I_{\text{rel}} \approx 0.00072$, whereas for $Re = 3023$ and $\Delta r, \Delta z = 1/60$, $I_{\text{rel}} \approx 0.00078$.

Although most of the solutions presented in this study reach a steady state (those which do not are noted), it is important to ensure that the model has temporal as well as spatial accuracy. In the parameter range where the flow reaches a steady state, Escudier (1984) reported that the time taken to reach this steady state from an impulsive start was typically tens of seconds. In that same parameter range, i.e. $1.5 \leqslant H/R \leqslant 2.0$ and $1000 \leqslant Re \leqslant 1500$, the numerical model reaches steady state for t between 500 and 700. In the case where $\nu = 4.5 \times 10^{-5}$ m^2/s and $R = 9.5 \times 10^{-2}$ m, which are the values in the experiments of Escudier (1984), we find $\Omega \approx Re/200$ and a 'spin-up' time to steady state of approximately 60 s. The numerical result is consistent with the experimental observations.

Escudier found experimentally that the flow undergoes a transition to unsteadiness at some critical combinations of Re and H/R and he has mapped this transition (figure 1). At the point where the flow becomes unsteady, the flow visualization technique is no longer able to give a clear picture of the flow characteristics. The present numerical solutions are found to accurately predict those flows which lead to

a steady state. This has given us confidence to investigate the transition to unsteadiness and this aspect of the flow is the subject of a further report which is in preparation. Preliminary results on the unsteady aspects of this flow are reported in Lopez (1989) and §4.

4. Results and discussion

Escudier (1984) has mapped a 'stability diagram' in the (Re, H/R)-plane delineating the regions where single, double and triple recirculation zones occur, together with the boundary between steady and oscillatory flows. This diagram is reproduced in figure 1. Some of the parameter values at which the flow has been simulated in this study are also indicated in the figure. Escudier has made available photographs of the recirculation zones and a number of these are reproduced here for comparison with the numerical solutions. The reader should be aware that in the photographs of the experiment, radial distances are reported to appear uniformly stretched by 8% due to refraction at the various interfaces.

The following is a brief description of the basic flow features.

The fluid, which completely fills the cylindrical container, is initially at rest. At $t = 0$, the bottom endwall is impulsively set to rotate at constant angular speed Ω. An Ekman boundary layer develops on the rotating disk with thickness of order $(\nu/\Omega R^2)^{0.5}$. This rotating boundary layer then acts as a centrifugal pump, sending fluid radially outwards in a spiralling motion while 'sucking' fluid into it from above. This pumping action of the boundary layer together with the presence of the cylindrical wall at $r = R$ sets up a secondary meridional circulation. The fluid pumped out of the Ekman layer spirals up the cylindrical wall, establishing a sidewall boundary layer. In time, fluid with angular momentum reaches the vicinity of the stationary top endwall, where it is turned and advected towards the centre. It spirals inwards creating a further boundary layer on the top endwall. On the stationary endwall the fluid separates at $r = 0$ and a concentrated central vortex is formed whose core size depends on the depth of the boundary layer from which it emerged. The fluid then spirals down this central vortex to be sucked back into the Ekman layer.

The experimental studies of this flow show that it undergoes a series of transitions as the two governing parameters, Re and H/R, are varied. The present study focuses on the development of the flow characteristics with Re and H/R up to the point where the flow no longer reaches a steady state. In particular, in the region of parameter space considered, i.e. $Re \leqslant 3000$ and $H/R \leqslant 3.5$, the flow is observed experimentally to remain axisymmetric and laminar, and for the most part to reach a steady state.

Figure 1 suggests that the flow characteristics depend critically on the Reynolds number. The numerical solutions suggest, however, that the basic dynamics of the central vortex are inertially driven and that viscous shears are small outside recirculation zones, boundary layers and away from the meridional shear layer in the bottom half of the cylinder which is caused by the strong turning at the corner $r = R, z = 0$. A comparison of the 'streamline' contours i.e. intersections of stream surfaces with the meridional plane, and contours of the angular momentum $\Gamma = rv$, on the meridional plane show that even at the relatively low value of $Re = 1000$ (see figure 2*a*) Γ is nearly constant on stream surfaces in the central region.

A more typical case where recirculation bubbles exist is $Re = 1994$. Figure 2(*f*) (ψ and Γ) and figure 3 ($\mathscr{H} = p/\rho + \frac{1}{2}(u^2+v^2+w^2)$) illustrate how the fluid acquires its angular momentum and total head in the Ekman layer on the rotating endwall and

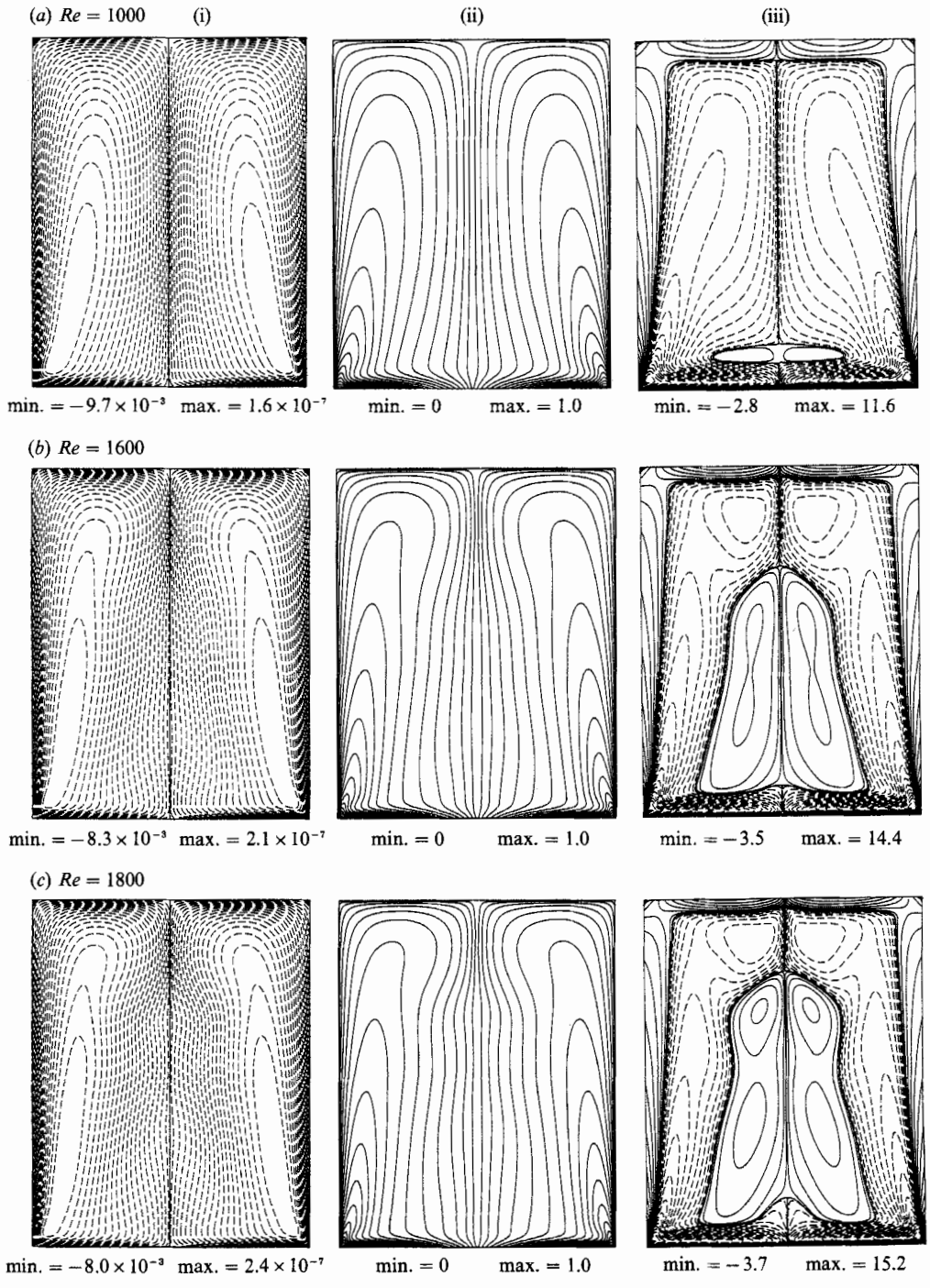

FIGURE 2(*a–c*). For caption see page 542.

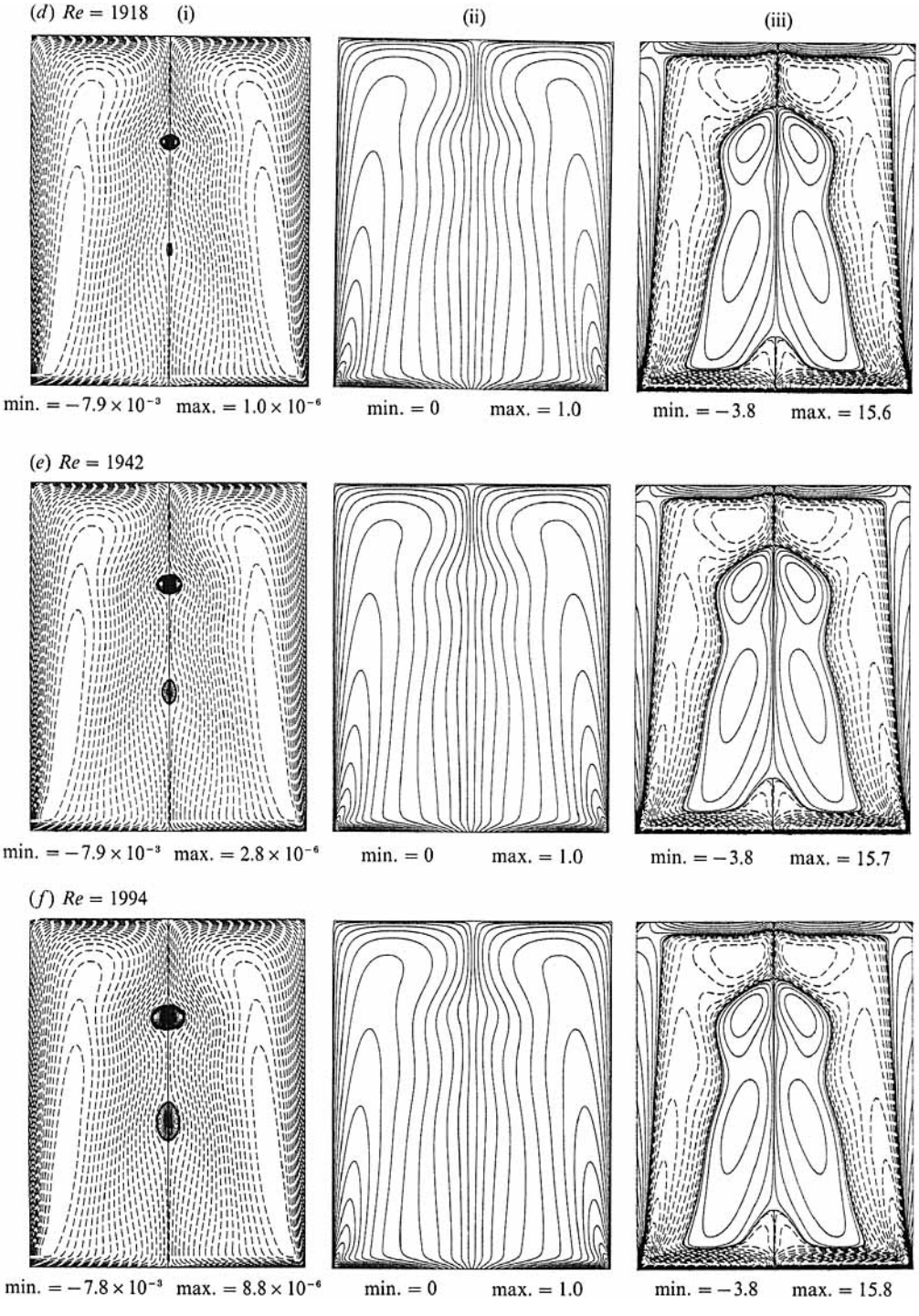

FIGURE 2(*d–f*). For caption see next page.

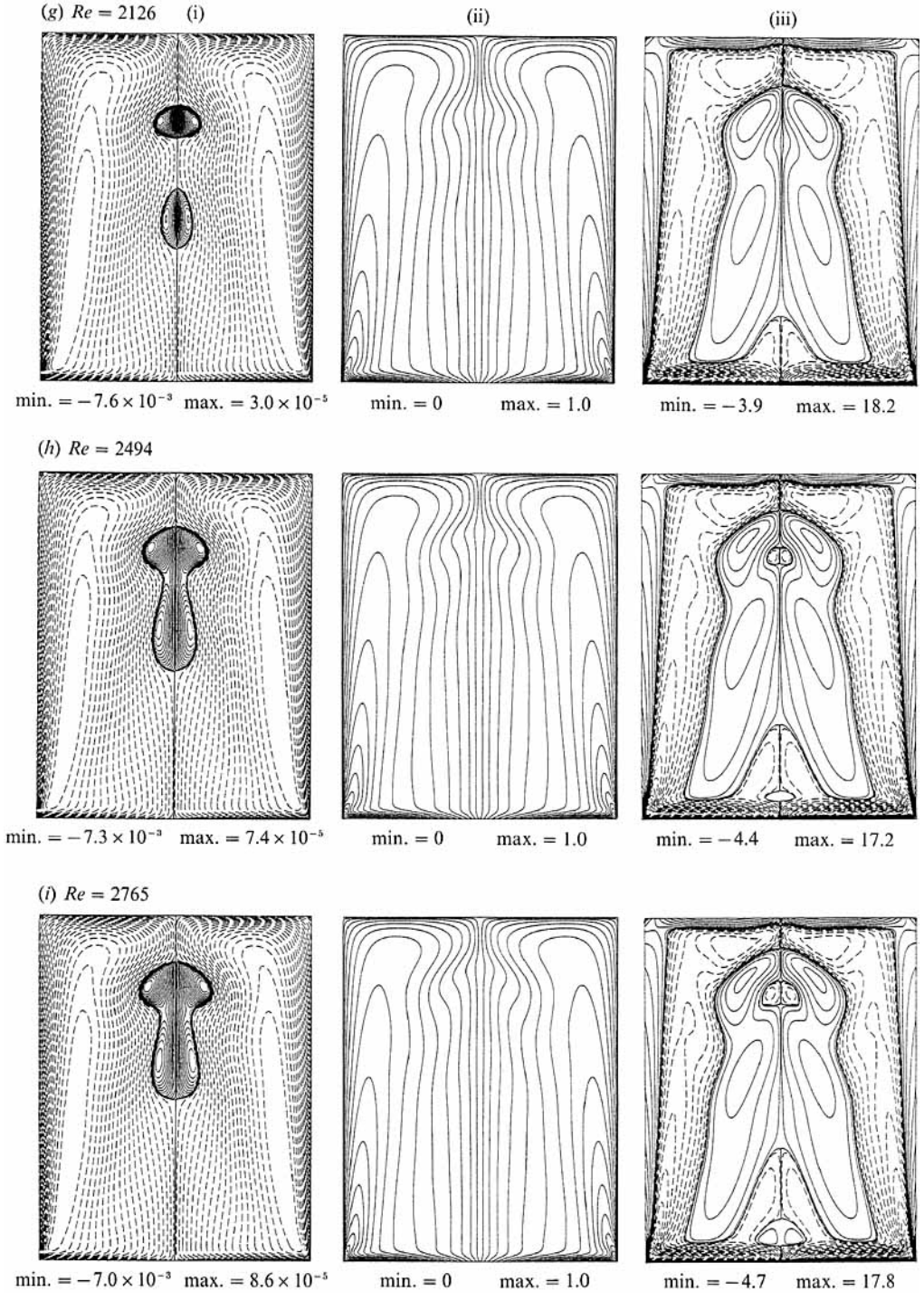

FIGURE 2. Contours of (i) ψ, (ii) Γ and (iii) η in the meridional plane for $H/R = 2.5$ and Re as indicated. The contour levels are non-uniformly spaced, with 20 positive and 20 negative levels determined by c-level(i) = Max(*variable*) × $(i/20)^3$ and c-level(i) = Min(*variable*) × $(i/20)^3$ respectively. All are plotted at $t = 1000$ by which time steady-state flow conditions have been reached, except for (i) which shows the time averages over $750 \leqslant t \leqslant 1000$ of an oscillatory flow.

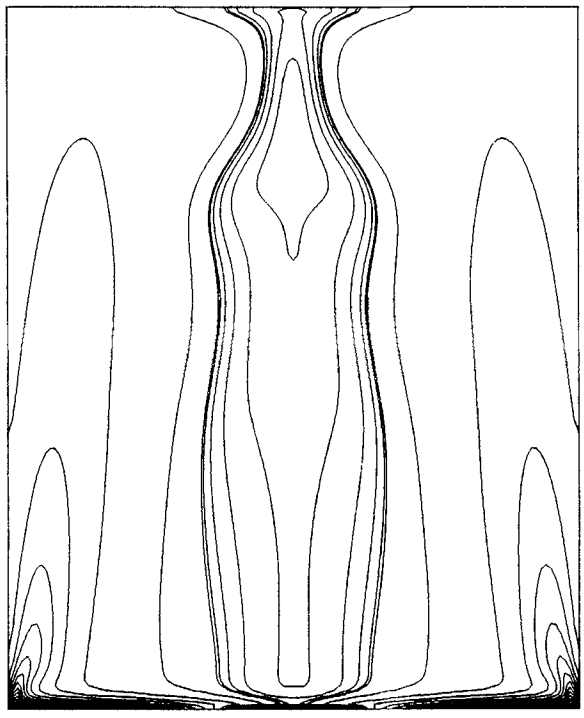

min. $= -3.8 \times 10^{-2}$ max. $= 6.5 \times 10^{-1}$

FIGURE 3. Contours of $\mathscr{H}$ in the meridional plane for $H/R = 2.5$ and $Re = 1994$. The contour levels are non-uniformly spaced, with 20 positive and 20 negative levels determined by c-level (i) = Max (*variable*) $\times (i/20)^2$ and c-level (i) = Min (*variable*) $\times (i/20)^2$ respectively. The contours are plotted at $t = 1000$, by which time steady-state flow conditions have been reached.

loses Γ and $\mathscr{H}$ in the viscous boundary layers on the stationary walls. In the central core region, however, a detailed comparison between the contours of ψ, Γ and $\mathscr{H}$ shows that Γ and $\mathscr{H}$ are approximately constant on stream surfaces, apart from those surfaces within and near to the recirculation bubbles where Γ and $\mathscr{H}$ are relatively small.

At $Re = 1000$, the curvature of the stream surfaces of the vortical fluid returning towards the lower rotating endwall does not change sign and the secondary meridional flow consists of a simple overturning motion. From the contour plots of the azimuthal vorticity (figure 2*a*(iii)), we find that η is positive in the boundary-layer regions and negative in the interior flow, consistent with a deceleration of the meridional flow in the boundary layers. Of particular interest is the small region of positive η just above the Ekman layer about the axis of symmetry.

It is interesting to examine the effect of increasing Re for the case in which $H/R = 2.5$. At $Re = 1600$ a waviness is evident in the stream surfaces of the central vortex as well as in the contours of Γ (see figure 2*b*). Comparing the Γ-contours of the two cases $Re = 1000$ and 1600, it is clear that a greater proportion of the fluid's angular momentum has been advected towards $r = 0$, in the upper boundary-layer region, leading to the formation of what appears to be a weak centrifugal wave in the higher-Re case. The contours of η at $Re = 1600$ (see figure 2*b*(iii)) are qualitatively similar to those at $Re = 1000$, but now the extrema in the values of the azimuthal vorticity have increased. The region of positive azimuthal vorticity in the interior of the flow

is extended considerably and roughly coincides with the region of 'wavy' stream surfaces.

The development of this standing wave on the vortex core region does not accord with the explanation given by Lugt & Abboud (1987), where it is suggested that the presence of the corner between the stationary sidewall and the stationary endwall (i.e. $r = R, z = H$) initiates the 'wavy motion' as the flow negotiates this corner and is then forced back towards the rotating disk, and that this 'wavy motion' is a viscous effect. The numerical results from this study clearly show that the 'wavy motion' is initiated (in the sense of increasing Re) well downstream of the viscous-boundary-layer flow and is associated with the development of a positive azimuthal component of vorticity. In Part 2, it is shown that the waves are driven by an inertial process, where the azimuthal component of vorticity plays an important role.

The above effects are further enhanced as Re is increased to 1800. Here the stream surfaces (figure 2*c*) clearly indicate the presence of a centrifugal wave with two periods and two bulges on the axis at approximately $\frac{1}{2}H$ and $\frac{2}{3}H$. Note, however, that the central vortex, as it emerges from the endwall boundary layer has stream surfaces that are almost parallel with a relatively large radial gradient, indicating the presence of a relatively large axial velocity in this core flow.

An increase in Re to 1918 crosses the boundary between no 'breakdowns' and 1–2 'breakdowns' on figure 1. The amplitude of the waves has increased and their wavelength decreased (see figure 2*d*). With the increased amplitude and decreased wavelength, the associated axial deceleration is large enough to cause the flow to stagnate under the crest of the wave. Within this stagnant region is found a near-spherical region of recirculating fluid which is termed a vortex breakdown bubble, i.e. a toroidal vortex centred on the axis of a columnar vortex. At this particular value of H/R there are two breakdown bubbles, the downstream bubble being considerably smaller and the recirculating flow within it slower than in the leading bubble.

For $H/R < 1.95$, both the experimental investigations of Escudier (1984) and our numerical calculations only identify single breakdown bubbles and for $H/R < 1.2$, no breakdown bubbles are found. Pao (1970) observed, in a related problem where the cylinder wall also rotates at the same angular speed as the disk, that for $H/R = 1.0$ and $Re > 500$ standing waves appear in the axial plane, and reported a similar dependence on Re for these waves as is found in this study. His experimental investigations include cases to $Re = 8600$ where the flow was reported to be steady, axisymmetric and laminar. However, he did not find any recirculating breakdown bubbles in his low-aspect-ratio ($H/R = 1.0$) container.

As Re is increased to 1942 (figure 2*e*), 1994 (figure 2*f*) and 2126 (figure 2*g*), very good agreement is found between the calculated stream surfaces and the observations of Escudier (1984). Some of these experimental observations are included for comparison with the numerical solutions in figure 4.

Although the length of the recirculation bubbles has grown with the increases in Re, the wavelength on the outer stream surfaces has been reduced. There remains a general trend that as Re is increased, the wavelength is reduced and the wave amplitude increased. The increase in the bubble diameters with Re is indicative of the increased wave amplitudes. The shortening of the wavelength is also consistent with the behaviour of the recirculation bubbles. As Re is increased, the region of near-parallel flow just after the vortex emerges from the boundary layer on the stationary endwall is shortened. This leads to a migration of the leading bubble towards this endwall. Note also that the distance between the two bubbles is progressively reduced as Re is increased.

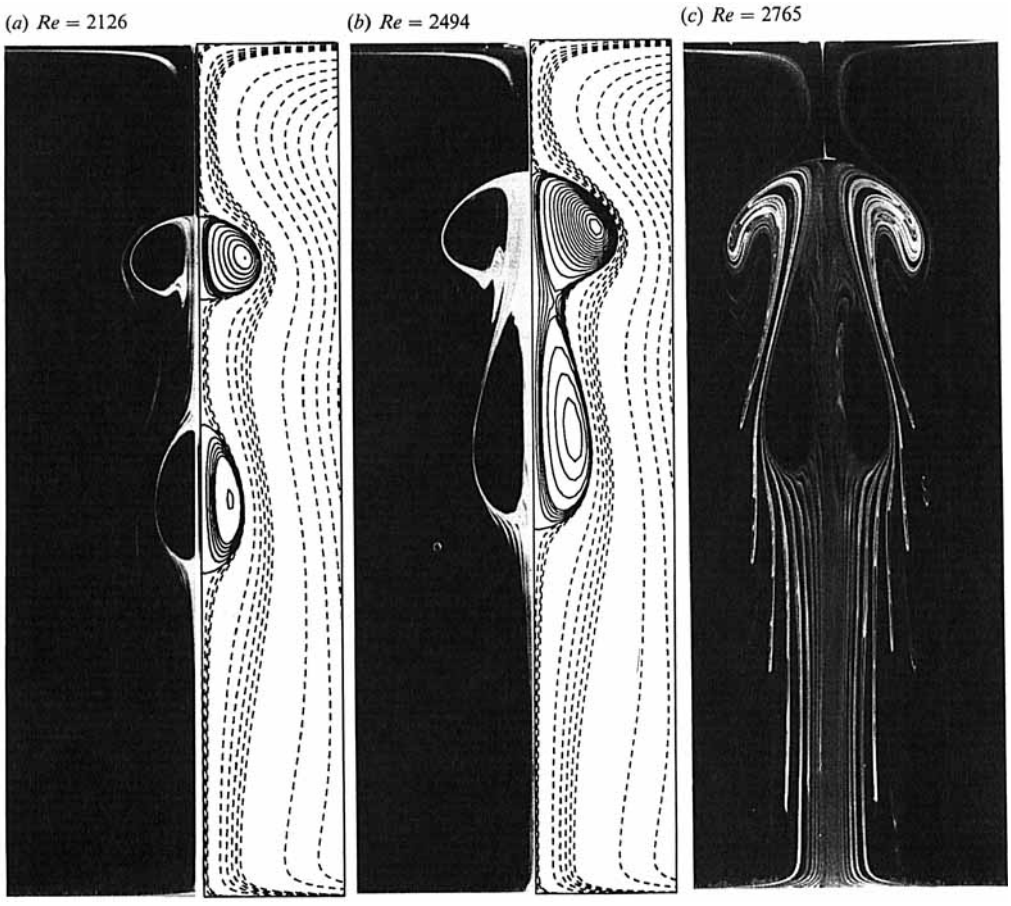

FIGURE 4. Flow structure of the recirculation zones for $H/R = 2.5$ and Re as indicated. (*a*), (*b*) Left halves of the figures are visualizations of the steady dye-lines and the right halves are the computed contours of the stream function at steady state for $0 \leqslant r \leqslant 5R/12$; (*c*) is a snap-shot of the unsteady dye-lines in an oscillatory flow. All photographs of the experimental visualization are reproduced by kind permission from M. P. Escudier.

The distribution of Γ is particularly interesting. For fluid in the central vortex that has emerged from the upper boundary layer, Γ is conserved on the stream surfaces for some axial distance over which the vortex remains concentrated. As a parcel of fluid spirals downstream past the breakdown region, there is a change in its angular momentum. When the fluid is first deflected radially outwards around the breakdown bubble, there is an increase in Γ, and when it is converged again around the downstream half of the bubble it loses some of this gain in angular momentum. The gradients in azimuthal velocity are large enough for the viscous stresses to effect these changes. Past the breakdown regions, the angular momentum distribution then corresponds to essentially solid-body rotation of the fluid. In essence, in these flows, the breakdown region is like a transition region from a concentrated vortical flow to solid-body rotation.

The details of the flow structure in the recirculation bubble are of particular interest in this study, even though their dynamical significance to the overall flow structure is secondary, because they provide an excellent test for the accuracy of the numerical solutions. It is possible to obtain very good flow visualizations of the

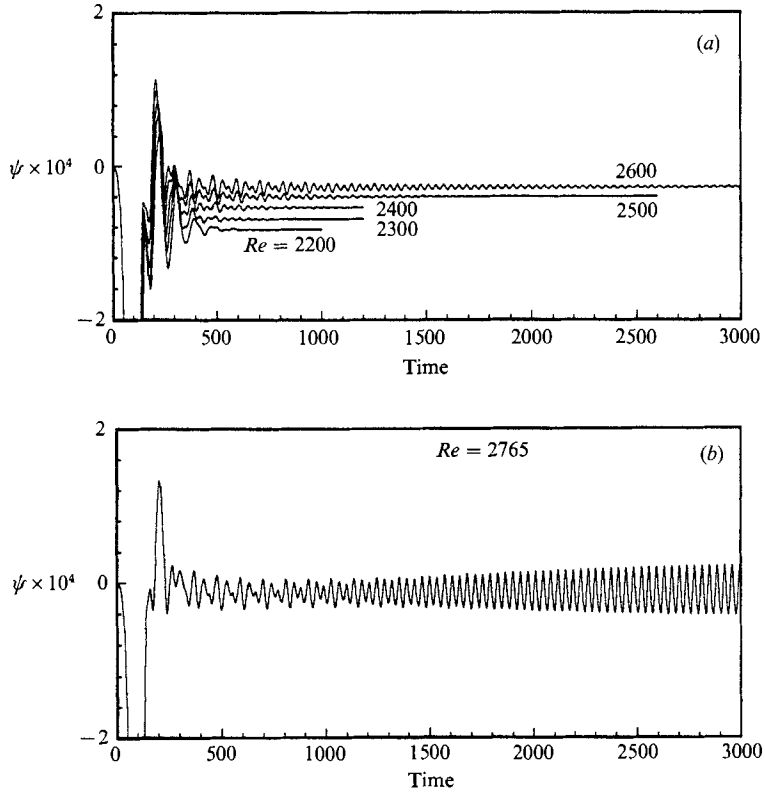

FIGURE 5. (*a*), (*b*). Time histories of $\psi \times 10^4$ at ($r = \frac{1}{6}R$, $z = \frac{2}{3}H$) for $H/R = 2.5$ and Re as indicated.

breakdown bubbles and their structure, and correspondingly of critical points and flow reversals. These features are much more demanding on a numerical model than the relatively simple structure of the outer flow.

Comparing in detail the structure of the recirculation regions as determined numerically and observed experimentally for $Re = 2126$ and $H/R = 2.5$ (figure 4*a*) we find very good agreement between the two. The structure of the upstream bubble is now clearly interpreted with the aid of the numerical solution. The leading stagnation point is well defined in the flow visualization; however, the downstream stagnation point is not as some dye finds its way into the bubble and some is swept past. As the fluid passes over the bubble at maximum diameter, the streamlines indicate a local acceleration of the meridional flow over the 'obstacle', i.e. bubble. As the fluid passes the bubble, it converges back towards the axis; however, the axial flow is now considerably slower than it was in its approach to the leading stagnation point. The dye photograph of the leading bubble shows a thin well-defined outer envelop with a rather broad, diffuse inner core. This is matched by the computed streamlines where they are contracted to the outer edge of the bubble and spread out within the interior. The same is true for the downstream bubble, although this information is not evident from the dye photograph since it appears that the dye is residing principally between a narrow band of streamlines which envelop the bubble, with virtually no dye inside the bubble. The computed streamlines indicate that the

recirculating flow in the downstream bubble is considerably slower than in the upstream bubble. Downstream of the second bubble, the enveloping dye streak is broad and is tapered as it approaches the Ekman layer. This behaviour is mirrored in the computed streamlines and may be interpreted as an axial acceleration of the flow, probably as a result of the boundary-layer suction.

This very close agreement between experimental observation and numerical calculation of the recirculation zones has not been achieved in every case, although in all cases the agreement has been very good. The reason is because the structure of the recirculation zones in the vicinity of parameter space where a recirculation zone just emerges is critically dependent on the value of Re. For example, the small change in Re from 1918 to 1942 (1.2%) results in a 25% increase in the diameter of the leading bubble and a 300% increase in the diameter of the second bubble, whereas the outer flow remains virtually unchanged (see figure 2*d*, *e*). Hence, a small percentage error in the estimate of Re can be responsible for a significant difference between the observed structure of the recirculation bubbles and their computed structure. Unfortunately, no uncertainty estimates on Re are available for the experimental observations. Escudier reports, however, that the temperature of the fluid was maintained at 25 °C $\pm$ 0.1 °C and the viscosity of the fluid varied by about 5% per °C. Hence a possible uncertainty of 0.5% exists in the estimate of Re due to the uncertainty in viscosity alone. For flows that are not so close to these critical parameter regions, the structure of the recirculation bubbles is not so variable with Re and a much closer agreement between the computations and the observations was found.

As the Reynolds number of the flow increases, the downstream bubble approaches the tail of the upstream bubble. Just beyond the value of Re at which the tail stagnation point of the upstream bubble coincides with the leading stagnation point of the downstream bubble, there is a topological change in the flow structure. For $H/R = 2.5$ this occurs for $2300 < Re < 2400$. This transition leads to a flow in which there are two stagnation points on the axis of symmetry defining the head and tail of the recirculation zone which encloses two distinct zones. These two zones are connected by a ring seen as two saddle points either side of the axis of symmetry in the meridional plane. In the case of $Re = 2494$, $H/R = 2.5$ (see figure 2*h*), this flow pattern is steady. The two critical streamlines, i.e. $\psi = 0$ enclosing the bubble and $\psi = 1.609 \times 10^{-6}$ defining the saddle points, are very close together around the outer envelope of the recirculation bubble, whereas there is a considerable gap between them near the axis of symmetry (see figure 4*b*).

At this point, it is worth noting the timescales of the evolution of these flows. As previously noted in §3, for the lower-Re cases, i.e. $1000 < Re < 2000$, the system reaches steady state after, following an impulsive start from rest, between 500 and 700 rotations of the bottom endwall. However, beyond $Re \approx 2000$, the time taken to reach steady state increases rapidly with Re, as indicated in figure 5(*a*) where time histories of the stream function at a point in the flow ($r = \frac{1}{6}R$, $z = \frac{2}{3}H$) are given for $2200 \leqslant Re \leqslant 2600$. The rapid increase in the time taken to reach steady state coincides with the transition in the structure of the recirculation bubbles, i.e. the coalescence of the two distinct bubbles present at lower Re. It is in the physical vicinity of the coalescence of the bubbles that the transient unsteadiness in the flow is most pronounced.

When Re is increased to 2765, the computed flow is unsteady and its structure oscillates between the structures typical of $Re = 2126$ and $Re = 2494$. Figure 2(*i*)

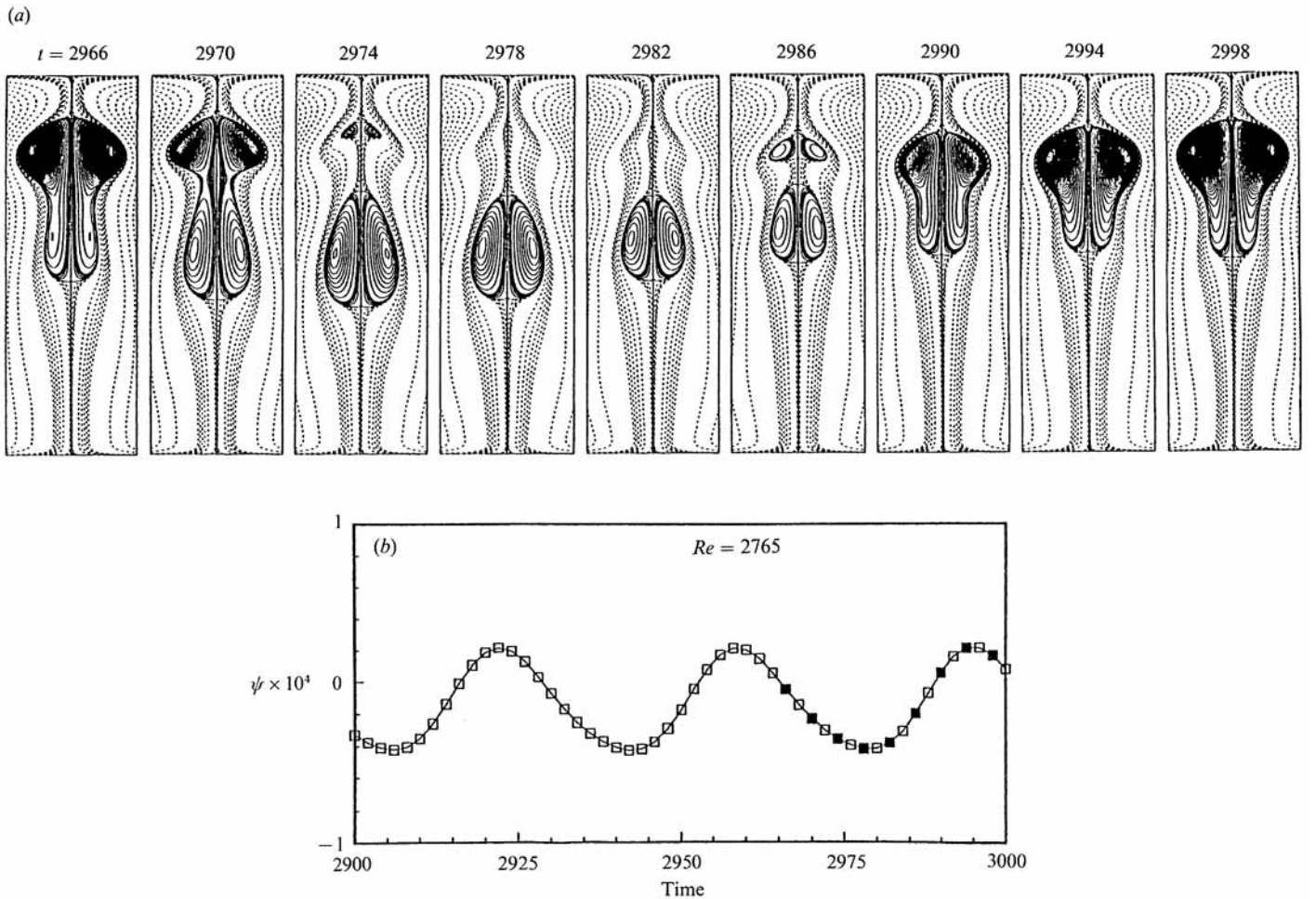

FIGURE 6. (*a*) Instantaneous streamlines in the central region $0 \leqslant r \leqslant 5R/12$ over one cycle of the periodic flow case $Re = 2765$, $H/R = 2.5$ at the indicated times. (*b*) Detail of the time history of $\psi \times 10^4$ in figure 5 (*b*). The filled squares correspond to the figures in (*a*).

shows time-averages of ψ, Γ and η. This figure may be compared with the 'snap-shot' of the experimental flow (figure 4*c*) which Escudier (1984) found to be steadily oscillating.

The flow visualization of this oscillatory flow, however, does not give a clear indication of the nature of the unsteadiness. Figure 5(*b*) shows the time history of the computed stream function at ($r = \frac{1}{6}R$, $z = \frac{2}{3}H$). After approximately 2750 revolutions of the endwall, the flow has settled down to a periodic state. The flow structure in the central core region over one cycle is given in figure 6(*a*) for $2966 \leqslant t \leqslant 2998$, and the time history for ψ at ($r = \frac{1}{6}R$, $z = \frac{2}{3}H$) is detailed in figure 6(*b*). The filled squares correspond to the instantaneous streamlines in figure 6(*a*). As is clear from the instantaneous streamlines (figure 6*a*), which was not clear from the unsteady dye-lines (figure 4*c*), the nature of the unsteadiness is due to the interaction between the two bubbles – coalescing and separating and coalescing etc. This might be regarded as consistent with the behaviour at lower Reynolds number where the time to reach steady state and the transient unsteadiness increase as the bubbles move closer together with increasing *Re*.

Note that the visualization of the unsteady dye-lines indicate that the flow upstream of the recirculation region is essentially steady and that the vortex core emerging from the endwall boundary layer is concentrated. These features are also present in the computed instantaneous streamlines. The 'mushroom' appearance of the upstream part of the recirculation zone in the unsteady dye-line figure might be understood from the fact that the vertical velocity changes sign within each cycle and leads to the complex folding of the dye-lines as shown in figure 4(*c*). A more detailed study of the streamlines and streaklines that are obtained in this unsteady flow is in progress.

In the region designated as 'three breakdowns' by Escudier (1984), numerical results were obtained for $H/R = 3.25$ and 3.5 as indicated in figure 1. In all cases considered, the downstream recirculation zone consists of two coalesced recirculation bubbles. The upstream breakdown region, however, remains separate. The numerical solutions for these 'triple breakdown' cases did not reach steady state after 1000 rotations of the bottom endwall. The parameter values for which these solutions were obtained are very near to those which, according to figure 1, separate steady and unsteady flows. Escudier (1984) observed that for parameter values in this region, steady conditions are only reached after a very long time (hundreds of rotations of the endwall). The amplitudes of the oscillations for the $H/R = 3.25$ cases are relatively small, consisting of variations in the values of the stream function of approximately 1%. The oscillations for the $H/R = 3.5$ cases were considerably larger, with the middle breakdown zone oscillating most. Figure 7(*b–d*) shows time-averaged contours of ψ, Γ and η for $Re = 3061$ and $H/R = 3.5$ and figure 7(*a*) is a photograph of the flow for the same values of the parameters. It is interesting to note Escudier's (1984) observation that the central recirculation zones for the $H/R = 3.5$ cases 'never develop into well defined regions', and this now appears to be due to these regions not quite reaching steady state.

5. Conclusion

A numerical solution of the axisymmetric Navier–Stokes equations has been obtained and used to examine the vortex breakdown phenomenon which occurs at certain values of the governing parameters for flows in an enclosed cylinder driven by a rotating endwall. The accuracy of the numerical solutions has been established

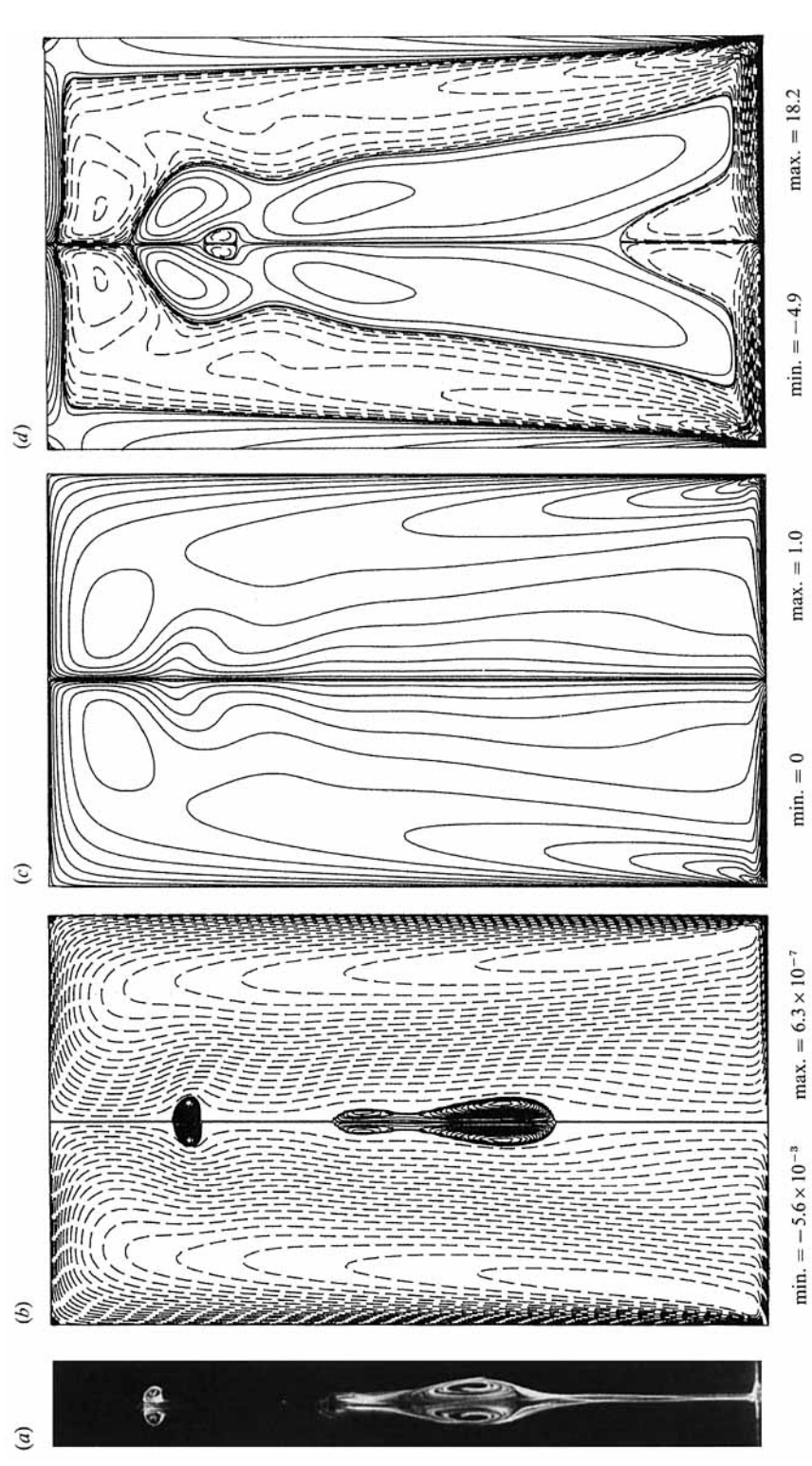

FIGURE 7. (*a*) Dye-lines, and computed contours of (*b*) ψ, (*c*) Γ and (*d*) η in the meridional plane for $H/R = 3.5$ and $Re = 3061$. The contour levels are non-uniformly spaced, with 20 positive and 20 negative levels determined by c-level(i) = Max(*variable*) × (i/20)^3 and c-level(i) = Min(*variable*) × (i/20)^3 respectively. The contours are of time averages over $750 \leqslant t \leqslant 1000$.

by varying the grid resolution and by determining the extent to which an integral identity is satisfied for the flow. Further, the numerical solutions are compared in detail with available experimental results, particularly dye-streak photographs of the flow. The extent of the agreement between the numerical solutions and the experimental results is critically examined and is found to be very good. Certain features of the flow, particularly connected with the development of recirculation zones and the onset of oscillatory flow, which could not be resolved from the visualization experiments, have been described. The numerical solutions also provide a clear picture of the topology of the flow, especially of the structure of the multiple recirculation zones.

In Part 2 of this study, the numerical solutions are analysed further and a physical understanding of the vortex breakdown phenomenon is gained.

REFERENCES

ARAKAWA, A. 1966 Computational design for long-term numerical integration of the equations of fluid motion: Two-dimensional incompressible flow. Part 1. *J. Comput. Phys.* **1**, 119–143.

BENJAMIN, T. B. 1962 Theory of the vortex breakdown phenomenon. *J. Fluid Mech.* **14**, 593–629.

BROWN, G. L. & LOPEZ, J. M. 1988 Axisymmetric vortex breakdown. Part 2. Physical mechanisms. *ARL Aero. Rep.* 174 *AR*-004-573.

BROWN, G. L. & LOPEZ, J. M. 1990 Axisymmetric vortex breakdown. Part 2. Physical mechanisms. *J. Fluid Mech.* **221**, 553–576.

DIJKSTRA, D. & HEIJST, G. J. F. VAN 1983 The flow between two finite rotating disks enclosed by a cylinder. *J. Fluid Mech.* **128**, 123–154.

ESCUDIER, M. P. 1984 Observations of the flow produced in a cylindrical container by a rotating endwall. *Expts Fluids* **2**, 189–196.

ESCUDIER, M. P. 1986 Vortex breakdown in technology and nature; and Vortex breakdown theories. *Von Karman Institute for Fluid Dynamics Lecture Series Programme.* 10. *Introduction to Vortex Dynamics. May* 1986, Lectures 9 and 10.

ESCUDIER, M. P. 1988 Vortex breakdown: observations and explanations. *Prog. Aerospace Sci.* **25**, 189–229.

ESCUDIER, M. P. & KELLER, J. J. 1983 Vortex breakdown: A two-stage transition. *AGARD CP*-342.

ESCUDIER, M. P. & ZEHNDER, N. 1982 Vortex flow regimes. *J. Fluid Mech.* **115**, 105–121.

FALER, J. H. & LEIBOVICH, S. 1978 An experimental map of the internal structure of a vortex breakdown. *J. Fluid Mech.* **86**, 313–335.

GRABOWSKI, W. J. & BERGER, S. A. 1976 Solutions of the Navier–Stokes equations for vortex breakdown. *J. Fluid Mech.* **75**, 525–544.

HALL, M. G. 1972 Vortex breakdown. *Ann. Rev. Fluid Mech.* **4**, 195–218.

HARVEY, J. K. 1960 Analysis of the 'vortex breakdown' phenomenon, Part 2. *Imperial College, Aero. Dept. Rep.* 103.

LEIBOVICH, S. 1978 The structure of vortex breakdown. *Ann. Rev. Fluid Mech.* **10**, 221–246.

LEIBOVICH, S. 1984 Vortex stability and breakdown: survey and extension. *AIAA J.* **22**, 1192–1206.

LOPEZ, J. M. 1988 Axisymmetric vortex breakdown. Part I: Confined swirling flow. *ARL Aero. Rep.* 173 *AR*-004-572.

LOPEZ, J. M. 1989 Axisymmetric vortex breakdown in an enclosed cylinder flow. In *11th Intl Conf. on Numerical Methods in Fluid Dynamics* (ed. D. L. Dwoyer, M. Y. Hussaini & R. G. Voigt). Lecture Notes in Physics, vol. 323, pp. 384–388. Springer.

LUGT, H. J. & ABBOUD, M. 1987 Axisymmetric vortex breakdown with and without temperature effects in a container with a rotating lid. *J. Fluid Mech.* **179**, 179–200.

LUGT, H. J. & HAUSSLING, H. J. 1973 Development of flow circulation in a rotating tank. *Acta Mech.* **18**, 255–272.

LUGT, H. J. & HAUSSLING, H. J. 1982 Axisymmetric vortex breakdown in rotating fluid within a container. *Trans. ASME* E: *J. Appl. Mech.* **49**, 921–923.

MILLER, M. J. & PEARCE, R. P. 1974 A three-dimensional primitive equation model of cumulonimbus convection. *Q. J. R. Met. Soc.* **100**, 133–154.

PAO, H.-P. 1970 A numerical computation of a confined rotating flow. *Trans. ASME E*: *J. Appl. Mech.* **37**, 480–487.

PECKHAM, D. H. & ATKINSON, S. 1957 Preliminary results of low speed wind tunnel tests on a Gothic wing of aspect ratio 1.0. *Aero. Res. Counc. CP*-508.

RONNENBERG, B. 1977 Ein selbstjustierendes 3-KomponentenLaserdoppleranemometer nach dem Vergleichsstrahlverfahren, angewandt für Untersuchungen in einer stationären zylindersymmetrischen Drehströmung mit einen Rückstromgebiet. *Max-Planck-Inst. Bericht* 20.

SARPKAYA, T. 1971 On stationary travelling vortex breakdown. *J. Fluid Mech.* **45**, 545–592.

SQUIRE, H. B. 1960 Analysis of the 'vortex breakdown' phenomenon. Part I. *Imperial College, Aero. Dept Rep.* 102.

SWEET, R. A. 1974 A generalized cyclic reduction algorithm. *SIAM J. Number. Anal.* **10**, 506–520.

VOGEL, H. U. 1968 Experimentelle Ergebnisse über die laminare Strömung in einen zylindrischen Gehäuse mit darin rotierender Scheibe. *Max-Planck-Inst. Bericht* 6.

WILLIAMS, G. P. 1967 Thermal convection in a rotating fluid annulus: Part 1. The basic axisymmetric flow. *J. Atmos. Sci.* **24**, 144–161.